


Wide-angle and high-efficiency acoustic retroreflectors enabled by many-objective optimization algorithm and deep learning models

Zhanhang Du and Jun Mei ^{*}*School of Physics, South China University of Technology, Guangzhou 510640, China*

(Received 5 September 2023; accepted 16 October 2023; published 3 November 2023)

By redirecting the incident wave energy back toward the source or sensor, retroreflectors mitigate signal losses, render a higher signal-to-noise transmission with improved sensing performance, and are highly desirable in acoustic applications such as remote sensing and detection, medical ultrasound imaging, and underwater communications. In this paper, we propose a different and efficient approach to realize a wide-angle high-efficiency retroreflector that is based on the design frame of acoustic metagrating. By integrating a many-objective optimization algorithm with a deep learning neural network, we construct a comprehensive and efficient optimization framework to intelligently design the metagrating so that its seven different diffraction orders work synergistically to realize the intended high-efficiency retroreflection functionality over a broad and continuous range of incident angles. Compared with the existing approaches based on corner cubes, Luneburg lenses, or dual-layer metasurfaces, the single-layer configuration of the retroreflector has a relatively simple unit-cell structure and can be easily extended to higher working frequencies. Both the proposed design paradigm itself and the high-performance retroreflector configuration may find applications in various scenarios including ultrasonic detection and imaging, music performance monitoring, and underwater communications.

DOI: [10.1103/PhysRevMaterials.7.115201](https://doi.org/10.1103/PhysRevMaterials.7.115201)

I. INTRODUCTION

Retroreflection refers to the physical phenomenon that an electromagnetic or sound wave is reflected back to its source along the direction antiparallel to the direction of incidence (i.e., $\theta_r = -\theta_i$). By redirecting the incident wave energy back toward the source or sensor, retroreflectors mitigate signal losses during the transmission process, rendering a higher signal-to-noise ratio (SNR) of the echo signal with improved sensing performance, thus contributing to realistic applications such as remote sensing and detection, high-SNR communications, and distributed sensor networks. As a kind of conventional retroreflector, the corner cubes [1] can realize the retroreflection function by letting the incident sound wave undergo multiple reflections with three mutually perpendicular intersecting plates and redirecting the incident wave back to its original direction. The cat's eye configuration, another conventional retroreflector composed of a focusing lens and a concave mirror placed at the focal point of the lens, is also a volumetric device [2]. These bulky and nonplanar retroreflection devices usually involve configurations of large size, curved shaped, and limited performance. However, low weight, cost effectiveness, and a planar configuration (easier for integration with other functional components) are desirable features for realistic applications. Thus, the development of a retroreflector with a planar structure, a smaller dimension scale, and higher reflection efficiencies over a wide range of incident angles is highly desired.

Acoustic metamaterials [3,4], a class of artificial materials with intendedly designed unit-cell structures and compositions, have attracted much attention in recent years due to their ability to control and manipulate the acoustic wave with intriguing functionalities beyond the capabilities of natural materials. The Luneburg lens [5,6] was designed to work in conjunction with an arcual mirror to enable acoustic retroreflection over a wide range of incident angles. On the other hand, the concept of a metasurface was proposed ~ 10 years ago, which was based on the generalized Snell's law and can be viewed as a two-dimensional (2D) version of metamaterials [7–11]. Metasurfaces have the ability to manipulate the phase and amplitude of the incident wave through their subwavelength unit-cells arranged in a planar configuration. Along this line, planar acoustic retroreflectors consisting of cascaded dual-layer metasurfaces [12,13], reconfigurable metasurfaces [14,15], and reflective metasurfaces with a curved surface shape [16] were constructed to demonstrate the interesting retroreflection effect.

However, for either Luneburg lenses or metasurface-based retroreflectors, their design process involves the discretization, fabrication, and assembly of deep subwavelength unit-cells, and slight misalignments of their internal structures can significantly reduce the efficiency of retroreflection and even result in the disappearance of the retroreflection effect. In addition, the Luneburg lens is based on an ideally continuously varying index profile over a circular area in 2D or a spherical volume in three dimensions, which is more difficult to implement than a planar device [5,6]. For the metasurface-based retroreflectors, the subwavelength internal structures or waveguide channels may induce thermal viscosity and bring about nonnegligible energy losses [17],

^{*}phjunmei@scut.edu.cn

especially for high-frequency acoustic waves. Furthermore, the impedance mismatch [18,19] between the incident and scattered waves will lead to a significant reduction in the scattering efficiency of metasurfaces, particularly for large steering angles. Obviously, the limitations of the existing approaches to retroreflectors are not beneficial to practical applications.

In parallel, the notion of metagrating was proposed recently as a design frame [20–22], which was based on the grating diffraction theory rather than the generalized Snell’s law. With properly designed unit-cells (i.e., meta-atoms), metagratings can redirect the incident wave energy exclusively to the desired direction with nearly unitary efficiency, even for large scattering angles [20–31]. In addition, the unit-cells of metagrating usually have a simpler structure than those of metasurfaces, avoiding the discretization of a continuous impedance profile with deep subwavelength structures, which is beneficial to sample fabrication and realistic applications. For these reasons, several metagrating-based acoustic retroreflectors were proposed and studied [32–43]. By utilizing periodically modulated grooves or cavities [32–40], C-shaped brass particles [41], or binary cells with π -phase difference [42] as the unit-cells of the metagratings, authors successfully demonstrated the retroreflection phenomenon and associated cloaking [33–35] or tweezing [39] effects for airborne and waterborne acoustic waves as well as elastic flexural waves [40]. However, these metagrating-based retroreflectors only work for a few fixed and discrete incident angles. Very recently, angular-adaptive retroreflectors based on reconfigurable metagratings or metasurfaces were demonstrated, but they are active devices requiring mechanically tuning the folding state [43] or use a pumping system or micromotors electrically controlled by a field programmable gate array [14,15] and are thus more complicated and expensive than passive devices.

In this paper, we aim to realize a passive, low-cost, low-profile, and wide-angle acoustic retroreflector based on a planar metagrating. To achieve an ideal retroreflection effect over a wide and continuous range of incident angles, an infinite number of diffraction orders of the metagrating is needed so that each incident angle corresponds to the same reflection angle enabled by one particular diffraction order. However, an infinite number of diffraction orders is obviously unfeasible, both theoretically and experimentally. Therefore, we adopt a different but efficient approach here and utilize a metagrating with finite diffraction orders. Our key idea is to relax the strict exact retroreflection condition ($\theta_{re} = -\theta_{in}$) to a more realistic and feasible quasiretroreflection one ($\theta_{re} \approx -\theta_{in}$). To be more specific, we utilize seven different diffraction orders of the metagrating to realize a wide-angle retroreflection functionality. To this end, we use a many-objective optimization (MOO) algorithm to handle the tradeoffs between seven conflicting optimization objectives and realize high-efficiency retroreflection over a broad and continuous range of incident angles ($13.7^\circ \leq |\theta_{in}| \leq 78.7^\circ$). Furthermore, we develop and train a predicting neural network (PNN) as an ultrafast deep learning model [44–48] with high prediction accuracy and combine it with the MOO algorithm to substantially accelerate the optimization process over the huge parameter space. With this comprehensive

MOO + PNN model, we can quickly find the globally optimized solutions that faithfully realize the intended retroreflection effect. The finally optimized configuration of the metagrating has a relatively simple structure and is easy to extend to higher working frequencies. Both the proposed design paradigm itself and the high-performance metagrating-based configuration may find applications in various scenarios such as remote sensing, ultrasonic detection and imaging, music performance monitoring, and underwater communications.

II. THEORY

According to the theory of grating diffraction, a plane wave incident at the angle of θ_{in} will be reflected by the grating into several diffraction channels, with each channel denoting a distinct reflection angle θ_{re} . From the diffraction analysis, the relationship between them can be expressed as $k_0 \sin \theta_{in} + m \frac{2\pi}{d} = k_0 \sin \theta_{re}$, where $k_0 = \frac{2\pi}{\lambda}$ is the wave number of the acoustic wave in the air background, d represents the periodicity of metagrating, and m is the diffraction order of the reflected wave. Here, m is an integer and can take only a few possible values because both the incident and reflected angles are confined within the range of $0^\circ \leq |\theta_{in(re)}| \leq 90^\circ$. To achieve the exact retroreflection effect, we should have $\theta_{re} = -\theta_{in}$, where θ_{re} and θ_{in} have opposite signs because the reflection and incident angles lie at the same side of the grating normal. To achieve the quasiretroreflection effect over a wide angular range, we should have $\theta_{re} \approx -\theta_{in}$, as schematically shown in Fig. 1(a).

For the m th diffraction order of the metagrating, the exact retroreflection condition $\theta_{re} = -\theta_{in}$ can be achieved if $\theta_{in} = \arcsin(\frac{-m}{2} \cdot \frac{\lambda}{d})$, where the diffraction order m is negative to enable the retroreflection. Without loss of generality, we set the periodicity of the grating as $d = 1$ m. To achieve the quasiretroreflection effect over a large angle range of $0^\circ \leq \theta_{in} \leq 80^\circ$, we assume the frequency of the acoustic wave be $f_0 = 1600$ Hz so that the corresponding wavelength in air is about $\lambda_0 = 0.21$ m. In this way, we need to consider ~ 9 or 10 diffraction orders of the reflected waves, which is a balanced value when considering both design difficulty and retroreflection efficiency. In principle, we can use a metagrating with a larger periodicity d for a given frequency so that more diffraction orders are involved in the reflected wave. However, too many diffraction orders that need to be simultaneously controlled lead to a highly challenging inverse design task and can result in a very complicated configuration of the unit-cell, as will be discussed later in more detail. In this paper, our primary aim is to demonstrate the principle and feasibility of the design paradigm and showcase the retroreflection functionality with an exemplary and simple implementation of the metagrating.

To be more specific, the relationship between the incident angle θ_{in} and reflection angle θ_{re} for different diffraction orders ($m = -1, -2, \dots, -9$) are plotted as dotted lines with different colors in Fig. 1(b). For example, the red dotted line represents the $m = -2$ diffraction order. The diagonal black dashed line denotes the exact retroreflection condition ($\theta_{re} = -\theta_{in}$), and its intersections (marked by yellow stars) with different diffraction orders indicate the discrete values of θ_{in} that can be exactly retroreflected. For

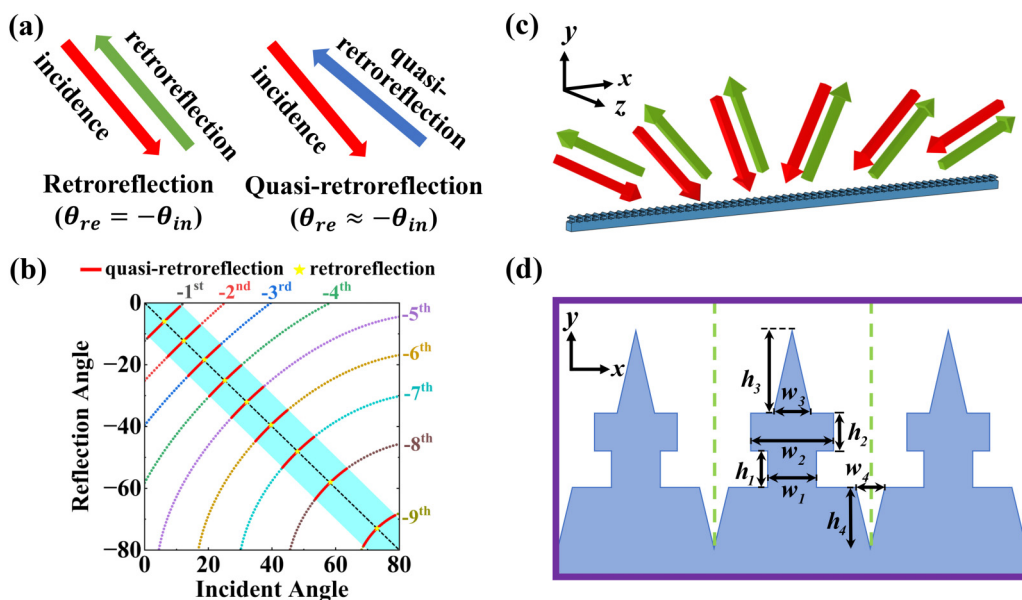


FIG. 1. Schematic of a metagrating-based retroreflector. (a) An illustration of the exact retroreflection and quasiretroreflection functionality. (b) The colored dotted lines represent the relationship between θ_{re} and θ_{in} for different diffraction orders ($m = -1, -2, \dots -9$) of the metagrating. The diagonal black dashed line represents the exact retroreflection condition ($\theta_{re} = -\theta_{in}$), and its intersections with the dotted lines (marked by yellow stars) imply that the exact retroreflection effect can be achieved only for several discrete incident angles. The light-blue-shaded region represents the quasiretroreflection range ($|\theta_{in} + \theta_{re}| \leq 10^\circ$), within which the dotted lines are marked by red lines. The continuity and/or overlap of red lines in terms of θ_{in} suggest the possibility of a wide-angle quasiretroreflection effect. (c) The functionality of a wide-angle retroreflector. (d) The unit-cell configuration of the metagrating, with each unit-cell consisting of a tree-shaped sound-hard material and a triangular groove.

example, with $m = -6$ in the exact retroreflection condition $\theta_{in} = \arcsin(\frac{-m}{2} \cdot \frac{\lambda}{d})$, we obtain $\theta_{in} = -\theta_{re} = 39.6^\circ$, which specifies the incident angle that can be exactly retroreflected by the -6 th diffraction order. Obviously, different diffraction orders m correspond to different θ_{in} , with $\theta_{in}^{exa} = 6.1^\circ, 12.3^\circ, 18.6^\circ, 25.2^\circ, 32.1^\circ, 39.6^\circ, 48.1^\circ, 58.2^\circ, 73.0^\circ$ being the incident angles of exact retroreflection enabled by $m = -1, -2, -3, -4, -5, -6, -7, -8, \text{ and } -9$, respectively.

To achieve a wide-angle retroreflection effect, as shown schematically in Fig. 1(c), we relax the exact retroreflection condition of $\theta_{re} = -\theta_{in}$ to a quasiretroreflection one of $|\theta_{in} + \theta_{re}| \leq 10^\circ$. That is to say, the reflection angle is allowed to span a narrow range around $-\theta_{in}$ with an upper limit $\theta_{re} = -\theta_{in} + 10^\circ$ and a lower limit $\theta_{re} = -\theta_{in} - 10^\circ$ when the incident angle is θ_{in} . Such quasiretroreflection regions are highlighted with a light blue background in Fig. 1(b). Red solid lines represent the θ_{in} and θ_{re} ranges that can realize the quasiretroreflection effect with different diffraction orders. For example, with $m = -6$ in $\theta_{re} = \arcsin(\sin \theta_{in} + m \frac{\lambda}{d})$ and $|\theta_{in} + \theta_{re}| \leq 10^\circ$, we can obtain 34.8° and 44.7° as the lower and upper limits, respectively, of the θ_{in} range that can achieve the quasiretroreflection effect enabled by the -6 th order.

With above diffraction analysis, we design an acoustic metagrating for airborne sounds, as illustrated schematically in Fig. 1(c), where each unit-cell (i.e., meta-atom) consists of a tree-shaped sound-hard structure and a triangular groove. The geometrical parameters w_1, w_2, w_3, w_4 and h_1, h_2, h_3, h_4 are explicitly marked in Fig. 1(d). The background material is air, with a mass density of 1.29 kg/m^3 and sound velocity

of 340 m/s . Without loss of generality, we aim to design a metagrating-based retroreflector working for a wide range of $13.7^\circ \leq \theta_{in} \leq 78.7^\circ$.

From the grating diffraction theory, for an incident wave within the range of $13.7^\circ \leq \theta_{in} \leq 23.6^\circ$, a high-efficiency quasiretroreflection effect can be realized by the -3 rd diffraction order. In a similar way, for incident waves within the ranges of $20.3^\circ \leq \theta_{in} \leq 30.2^\circ, 27.3^\circ \leq \theta_{in} \leq 37.2^\circ, 34.8^\circ \leq \theta_{in} \leq 44.7^\circ, 43.3^\circ \leq \theta_{in} \leq 53.2^\circ, 53.6^\circ \leq \theta_{in} \leq 63.5^\circ, \text{ and } 68.8^\circ \leq \theta_{in} \leq 78.7^\circ$, it is possible to realize the quasiretroreflection functionality with the -4 th, -5 th, -6 th, -7 th, -8 th, and -9 th diffraction orders, respectively. In this way, a broad-angle retroreflection functionality can be realized by stitching together each range of θ_{in} enabled by different diffraction order m .

To this end, we use an intelligent optimization algorithm to design the metagrating-based retroreflector, where the reflection efficiency at the seven discrete incident angles ($\theta_{in}^{exa} = 18.6^\circ, 25.2^\circ, 32.1^\circ, 39.6^\circ, 48.1^\circ, 58.2^\circ, \text{ and } 73.0^\circ$) at seven diffraction channels ($m = -3, -4, -5, -6, -7, -8, \text{ and } -9$) are set as the optimization objectives. We note that, although only seven reflection efficiencies at seven incident angles are being optimized, the resultant reflection efficiencies at other incident angles are also being optimized at the same time, as will be shown later. In short, we need to optimize eight geometrical parameters to simultaneously handle seven optimization objectives. Obviously, with eight parameters to be simultaneously optimized, the parameter space is huge.

For the traditional single-objective optimization algorithms such as the genetic and particle swarm optimization algo-

gorithms, usually only a single design objective needs to be considered. Although we can construct an average function such as $R_{\text{avg}} = \sum_{m=-3}^{-9} c_m R_m$ (c_m is the adjustable weight factor, and R_m is the reflection efficiency for the m th diffraction order, with its definition and calculation method detailed in Appendix A) to simplify the original multiobjective targets into a single-objective one, such a brute-force simplification would lose important information in the objective space and make the algorithm stuck in a local minimum instead of finding a global minimum [49]. Therefore, the traditional single-objective optimization algorithms are not suitable for the design of a wide-angle retroreflector. To this end, we utilize a MOO algorithm to simultaneously handle seven distinct objective functions and avoid getting trapped in local optimal solutions.

MOO is a type of vector optimization that has been applied in many fields of science where optimal decisions need to be taken in the presence of tradeoffs between two or more conflicting objectives. For a nontrivial MOO problem, no single solution exists that simultaneously optimizes each objective. In that case, the objective functions are said to be conflicting. A solution is called nondominated or Pareto optimal if none of the objective functions can be improved without degrading some of the other objective values. Without additional subjective preference information, there may exist several Pareto optimal solutions, all of which are considered equally good.

In this paper, we employ NSGA-III [50], an advanced and powerful MOO algorithm that is predominantly suitable for addressing optimization challenges characterized by multiple conflicting objectives. The fundamental steps of NSGA-III encompass nondominated sorting, reference-point-based sorting mechanism, tournament selection operations, as well as crossover and mutation operations. In each iteration of NSGA-III, tournament selection is employed to pick the superior individuals as parents, followed by crossover and mutation operations to construct the new individuals (offspring). Subsequently, nondominated sorting is applied to rank the population composed of both offspring and parent individuals based on the performance on specific targets. In addition, the reference-point-based sorting mechanism contributes to maintain the distribution of solutions, ensuring a uniform spread of solutions along the Pareto front, thereby mitigating issues related to local convergence. Compared with other MOO algorithms such as NSGA-II and MOPSO, NSGA-III is particularly suited for MOO problems with three or more objective functions.

As mentioned previously, the inverse design of a metagrating-based retroreflector can be formulated as a MOO problem with seven distinct objectives, i.e., simultaneously maximizing the reflection efficiencies along seven diffraction channels ($m = -3, \dots, -9$). Here, we use COMSOL Multiphysics for the calculation of the reflection efficiencies. Then the loss functions can be written as $L_m = (1 - R_m)^2$, respectively, and the minimization of L_m leads to the maximization of R_m . Obviously, they conflict with each other due to the law of energy conservation, i.e., $\sum_m R_m = 1$. Thus, this problem is particularly suitable for NSGA-III. In this stage, we set the population size as 300. After conducting 30 000 COMSOL simulations with a time cost of 16 h, NSGA-III finds one set

of Pareto solutions that contains at least one optimized solution with high-reflection efficiencies for all related diffraction orders. Their retroreflection efficiencies are relatively high (e.g., $R_m > 0.5$ for all m) but still far from perfect, simply because the parameter space is too big for NSGA-III to find the global minimum in one go. Thus, we called them suboptimized or nearly optimized solutions. Interestingly, such suboptimized solutions are often concentrated as clusters, where high-quality solutions with high-reflection efficiencies are distributed within several small regions in the parameter space. Repeating this optimization process with different initial guesses, we find 23 suboptimized solutions in the parameter space. In the optimization process, for each individual, we need to accurately calculate its reflection spectra of multiple diffraction orders over a wide angular range, which is indeed time consuming when using COMSOL. Following this way, it takes about $n_s \times 16$ h for us to find n_s suboptimized solutions. Since the (eight-dimensional) parameter space is huge, these suboptimized solutions are usually not globally optimized solutions, even after we repeat the above process many times. Thus, we must find an alternative way to greatly enhance the optimization efficiency.

To this end, we develop and train a PNN and combine it with NSGA-III to work synergistically to accelerate the optimization process. Given enough data, the PNN can be trained to learn the nonlinear relationship between the design parameters of the metagrating (geometrical parameters such as $w_{1,2,3,4}$ and $h_{1,2,3,4}$) and their response functions (the reflection efficiency R_m as a function of θ_{in}). After training well, the PNN can quickly and accurately predict the reflection response from the geometrical parameters, serving as an efficient predicting model with minimal prediction errors. In this way, significantly enhanced calculation efficiency can be achieved by PNN, three orders of magnitude faster than COMSOL. Therefore, even though it takes some time to develop and train the PNN, in total, we can achieve greatly improved optimization efficiency when integrating the PNN with NSGA-III.

As mentioned above, each meta-atom of the metagrating is characterized by eight design parameters, which implies a huge parameter space (or design space). Training a PNN that can thoroughly and completely map the whole design space to the response space would demand a staggering amount of data, rendering it impractical. However, in applying NSGA-III, we notice that high-quality data (those with high-retroreflection efficiencies) tend to cluster around smaller regions in the parameter space, while other regions are filled with low-quality data and can be safely disregarded. Thus, excluding those spacious low-value regions can greatly enhance the optimization efficiency and is beneficial to the searching of global optimized solutions.

Along this routine map and starting from the 23 suboptimal solutions previously found, we develop and train 23 PNNs and then integrate it with NSGA-III to design the retroreflector more efficiently. Firstly, we define a small region in the parameter space around each suboptimal solution, i.e., $\{D_i | d_{\text{opt},i} - 0.05 \times d_{\text{span}} \leq d \leq d_{\text{opt},i} + 0.05 \times d_{\text{span}}\}$, where d_{span} represents the diameter of the geometrical parameter (i.e., the difference between the upper and lower limits), and $i = 1, \dots, 23$ denotes the i th region. Within each region D_i ,

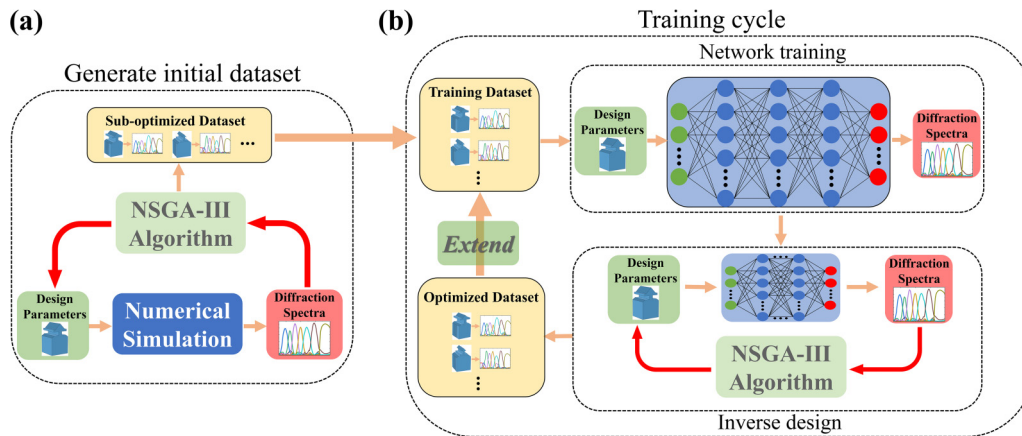


FIG. 2. (a) In the first stage, we use NSGA-III and COMSOL to perform the many-objective optimization. After conducting 30 000 COMSOL simulations, NSGA-III can find one set of Pareto solutions. Repeating this optimization process, we find 23 suboptimized solutions and 23 small regions in the parameter space. (b) In the second stage, we develop and train 23 predicting neural networks (PNNs) and integrate it with NSGA-III to accomplish the inverse design task. An initial training dataset of the PNNs is formed by utilizing the data in the 23 small regions. Then we concurrently use NSGA-III to generate new solutions, use COMSOL to evaluate their reflection response, and iteratively extend the training dataset of PNNs with high-quality data. In each cycle of the inverse design process, we use NSGA-III to continuously and intelligently explore the 23 small regions and search for high-quality data with higher reflection efficiencies and select the best ones and supplement them into the training set to iteratively retrain the PNNs. In this way, the training dataset can be iteratively updated and refined in each cycle, leading to the continuously accumulation of high-quality data. Repeating such a cycle 10 times, we finally find the sets of optimized solutions that can produce the desired retroreflection functionality. At the same time, we obtain 23 PNNs with a high prediction accuracy. Using this NSGA-III + PNN framework, the design efficiency of the retroreflector can be greatly enhanced.

we randomly sample 1000 sets of design parameters and calculate their diffraction responses, which takes ~ 40 min for each D_i . For simplicity, we call each set of design parameters and the diffraction response as one datum. These 1000 data are utilized as the initial training data of one PNN. There are 23 PNNs for 23 regions. Each PNN is a fully connected neural network consisting of four hidden layers with 500–500–500–500 neurons, where the rectified linear unit is used as the activation function. The input layer contains eight neurons, representing the eight design parameters of each meta-atom, while the output layer consists of seven neurons, denoting the retroreflection efficiencies along seven diffraction channels. The activation function of the output layer is a sigmoid function to ensure that the output values of the PNN (i.e., retroreflection efficiencies) fall within a reasonable range between 0 and 1. For the training of the PNNs, we employ the adaptive moment estimation algorithm optimizer to iteratively update the weights and biases of the neurons. The objective is to minimize the mean absolute error loss function, denoted as $L = \frac{1}{N} \sum_{n=1}^N |S_{\text{simu}}^{(n)} - S_{\text{pred}}^{(n)}|$, where $|S_{\text{simu}}^{(n)} - S_{\text{pred}}^{(n)}|$ represents the absolute difference between the COMSOL simulation results $S_{\text{simu}}^{(n)}$ and the predicted values of the PNN $S_{\text{pred}}^{(n)}$, with n denoting each datum. With the learning rate and batch size set as 0.001 and 64, respectively, the training error of the PNN is effectively minimized to an ideal value of ~ 0.02 , with the typical training time being ~ 6 min. Compared with COMSOL, a well-trained PNN can provide highly accurate predictions with small errors in the diffraction efficiencies. Therefore, we can replace the rigorous COMSOL simulations with the PNN model and concurrently use the PNNs and NSGA-III for the inverse design of the retroreflector.

Next, we integrate NSGA-III with the PNNs to accomplish the inverse design task of the metagrating. At this stage, the population size of NSGA-III is set as 1000. We use the previously trained PNNs to predict the response function of each individual, and the predicted reflection response is feedback to NSGA-III to generate new sets of parameters and further optimize the response function. After 200 000 times of PNN predictions, the optimization algorithm concludes and outputs the optimized solutions; among them, 300 solutions with the best performance are saved. We repeat the above process five times with different initializations of NSGA-III and then select the 300 best data with the highest diffraction efficiency R_{avg} . The above generation and selection process costs ~ 30 min.

Then we calculate the reflection efficiencies of these 300 high-quality solutions with COMSOL and add them to the training dataset of each PNN. Each iteration of the inverse design process is illustrated in Fig. 2(b). After the 300 data are added, the PNN is retrained, and it follows that the prediction precision of PNN is further improved. We repeat this iteration 10 times and each time add 300 data to the training set of PNN. With the original 1000 data, at the end, a big set of 4000 high-quality solutions are found in each D_i . In total, we have 23×4000 high-quality data for all 23 D_i regions, which constitute the ultimate training data of the PNNs. In this way, the prediction accuracy of the PNNs can be iteratively improved. Finally, the PNNs can replace COMSOL with negligible prediction errors. With the help of the high-accuracy PNNs, we can greatly improve the optimization efficiency of NSGA-III. As a result, a set of globally optimized solutions can quickly be found with this comprehensive NSGA-III + PNN framework, where the time cost is much less than the conventional NSGA-III + COMSOL model.

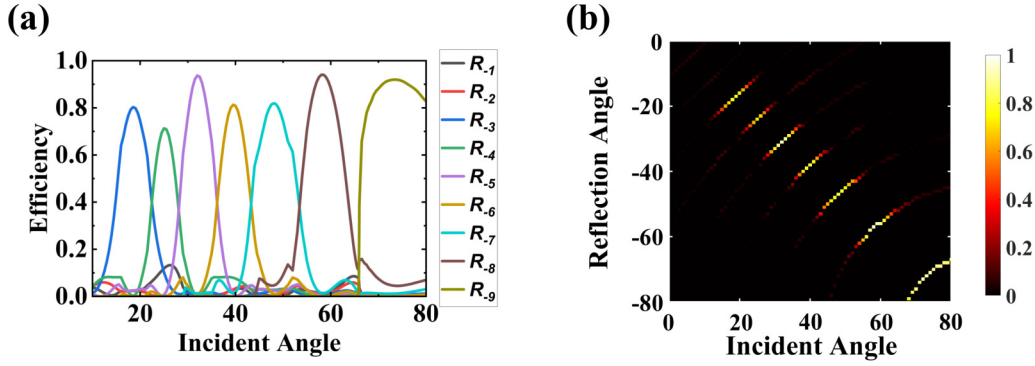


FIG. 3. The retroreflection response of the globally optimized solution. (a) The reflection efficiencies for the $m = -1, \dots, -9$ diffraction. Each order achieves its maximum reflection efficiency at the exact retroreflection angle, with the reflection efficiencies being 78.8, 72.1, 92.8, 82.4, 82.2, 94.7, and 91.7% for $\theta_{\text{in}}^{\text{exa}} = 18.6^\circ, 25.2^\circ, 32.1^\circ, 39.6^\circ, 48.1^\circ, 58.2^\circ, \text{ and } 73.0^\circ$, respectively. (b) The two-dimensional (2D) map of the diffraction response, with bright and dark colors representing high- and low-reflection efficiencies, respectively, indicating a wide-angle retroreflection effect for $13.7^\circ \leq \theta_{\text{in}} \leq 78.7^\circ$.

III. RESULTS

By utilizing the NSGA-III + PNN framework, we find the following globally optimized solutions: $w_1 = 0.0849m$, $w_2 = 0.4340m$, $w_3 = 0.1430m$, $w_4 = 0.2020m$, $h_1 = 0.0922m$, $h_2 = 0.2248m$, $h_3 = 0.3553m$, and $h_4 = 0.7184m$. The corresponding diffraction efficiency spectra as a function of θ_{in} are plotted in Fig. 3(a). Figure 3(b) shows the relationship between θ_{re} and θ_{in} , with bright colors presenting high-reflection efficiencies, which is consistent with the desired wide-angle retroreflection functionality shown in Fig. 1(b). The optimization reflection efficiencies are 78.8, 72.1, 92.8, 82.4, 82.2, 94.7, and 91.7% at the exact retroreflection angles of $\theta_{\text{in}}^{\text{exa}} = 18.6^\circ, 25.2^\circ, 32.1^\circ, 39.6^\circ, 48.1^\circ, 58.2^\circ, \text{ and } 73.0^\circ$, respectively. The average retroreflection efficiency over these seven incident angles is 85.0%, being very high.

To demonstrate the retroreflection effect, in Fig. 4, we show the full-wave numerical simulation results. Figures 4(a)–4(g) show the scattered pressure field when a Gaussian beam is incident along the exact retroreflection angles. Nearly perfect retroreflection effect can be observed. The corresponding far-field radiation patterns are shown in Figs. 4(h)–4(n), where the blue contours show the far-field radiation patterns when acoustic beams are incident along the red arrow directions. The blue polar plots of the reflected power verify again the exact retroreflection effect.

Furthermore, the reflection efficiencies along other incident directions are also high, with the reflective direction being very close to the incident direction. As shown in Fig. 3(a), the reflection efficiency spectra of $m = -3, -4, -5, -6, -7, -8, \text{ and } -9$ orders are distributed evenly within the range of $13.7^\circ \leq \theta_{\text{in}} \leq 78.7^\circ$, and they raise to peaks one after another with increase of θ_{in} . In this way, we achieve a high-retroreflection efficiency $R_m (>40\%)$ for any θ_{in} within the above continuous angular range, demonstrating a continuous and wide-angle retroreflection effect.

Some examples are shown in Fig. 5, where Figs. 5(a)–5(f) display the scattered pressure field resulting from Gaussian beams incident at angles of $20^\circ, 30^\circ, 40^\circ, 50^\circ, 60^\circ, \text{ and } 70^\circ$, respectively, where $\theta_{\text{diff}} = |\theta_{\text{in}} + \theta_{\text{re}}|$ represents the angular difference between the incident and reflective directions.

Here, θ_{diff} takes the values of $2.81^\circ, 4.22^\circ, 0.79^\circ, 3.82^\circ, 3.49^\circ, \text{ and } 6.61^\circ$, respectively, being very small for all cases. The corresponding far-field radiation patterns are shown in Figs. 5(g)–5(l), where the green-shaded regions represent the quasiretroreflection condition, i.e., $|\theta_{\text{in}} + \theta_{\text{re}}| \leq 10^\circ$. Thus, with a passive and intelligently designed metagrating, we have successfully realized a high-efficiency retroreflector for a broad incident angle range of $13.7^\circ - 78.7^\circ$.

In the demonstrations of Figs. 4 and 5, the Gaussian beams are incident from the left-hand side with a positive incident angle θ_{in} . However, we want to note that the retroreflector works equivalently for negative incident angles. Since the meta-atom shown in Fig. 1(d) has mirror symmetry with respect to the grating normal, it is easy to infer that, when the Gaussian beams are incident from the right-hand side, the same retroreflection functionality can be obtained. Thus, the retroreflector works efficiently over an angular range of $-78.7^\circ \leq \theta_{\text{in}} \leq -13.7^\circ$ and $13.7^\circ \leq \theta_{\text{in}} \leq 78.7^\circ$.

Here, we do not optimize the reflection performance for $|\theta_{\text{in}}| < 13.7^\circ$. The reason is that a small-angle reflection requires a very large number of diffraction channels and is not easy to implement with metagrating due to the underlying mechanism of grating diffraction. In this regard, the small-angle reflection performance of the retroreflector is presented in Appendix B.

As shown in Fig. 1(d), the unit-cell of the metagrating is composed of a tree-shaped sound-hard material and a triangular groove. The reason why such a specific shape is chosen is given in Appendix C.

Furthermore, the comprehensive MOO + PNN model provides us the flexibility that multiple optimized solutions can be found simultaneously, and all of them have overall satisfying retroreflection performance. To this end, we compare one locally optimized solution with the globally optimized solution in Appendix D.

IV. DISCUSSION

We note that the realization of a wide-angle retroreflector is enabled by considering only seven optimization objectives

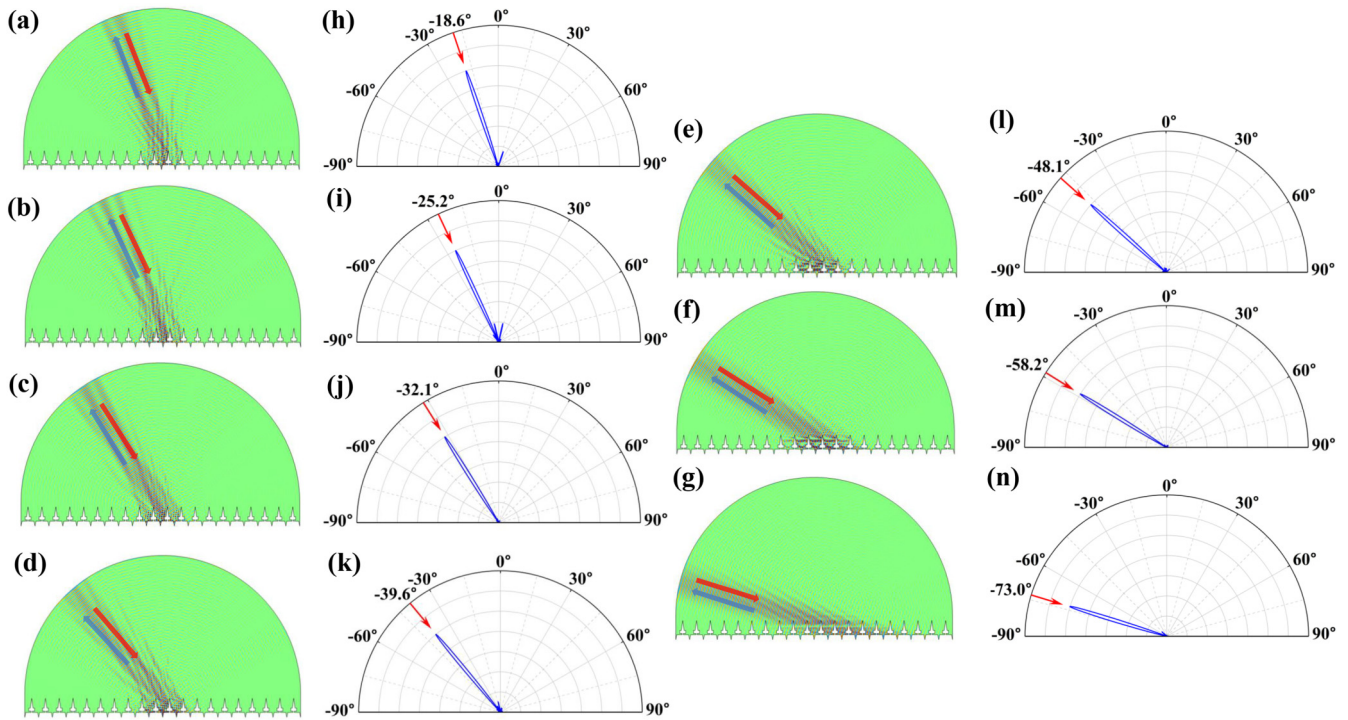


FIG. 4. The performance of the metagrating-based retroreflector. (a)–(g) Gaussian beams are incident at $\theta_{in}^{exa} = 18.6^\circ, 25.2^\circ, 32.1^\circ, 39.6^\circ, 48.1^\circ, 58.2^\circ$, and 73.0° , respectively, and are reflected back along the same path. The directions of the incident reflected wave beams are shown by red and blue arrows, respectively. (h)–(n) The corresponding far-field radiation patterns. Red arrows indicate the incident directions. Blue contours point to the reflective directions, with their amplitudes proportional to the far-field reflection intensity.

at seven discrete incident angles, with no need to consider the reflection efficiencies at other incident angles in the range of $13.7^\circ \leq |\theta_{in}| \leq 78.7^\circ$. The reasons are as follows. On one hand, if more optimization objectives (such as the reflection efficiencies at 30 or 50 different incident angles) are involved, the MOO algorithm would need much more iterations to converge to an optimized solution with satisfying

performance, which imposes a huge cost of time and becomes impractical. To solve the inverse design problem with limited computational resources and a limited time cost, we only select the reflection efficiencies at seven angles as the optimization objectives. It turns out that the metagrating configuration is very suitable for this purpose. Due to the physical mechanism of grating diffraction, the reflected wave beams

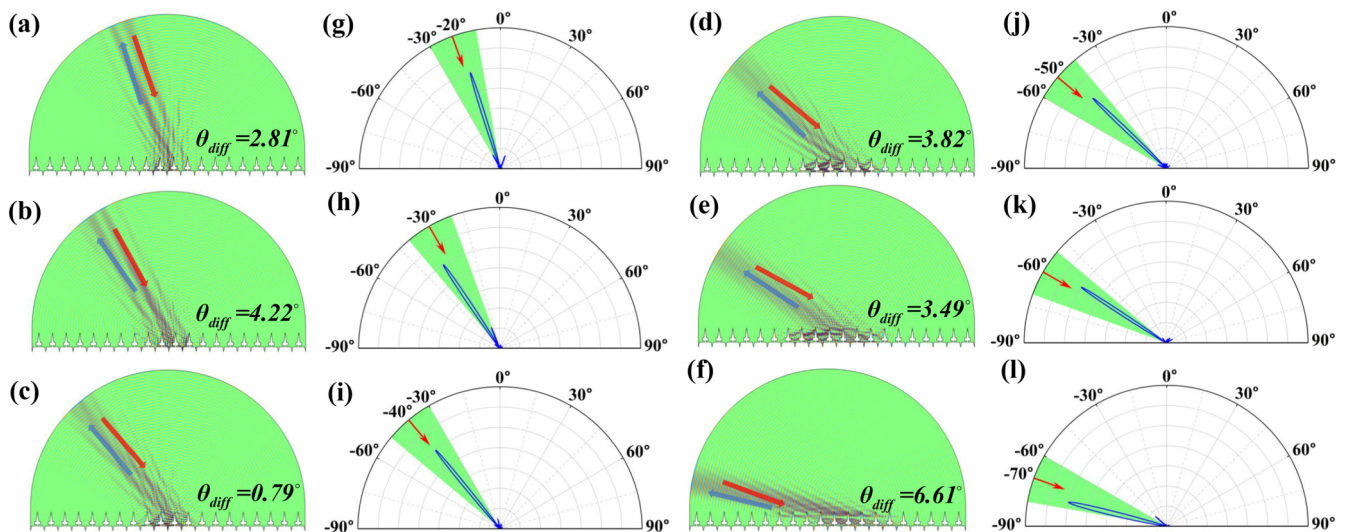


FIG. 5. The quasiretroreflection effect over a continuous and wide range of incident angles. (a)–(f) show the scattered pressure field when Gaussian beams are incident at $20^\circ, 30^\circ, 40^\circ, 50^\circ, 60^\circ$, and 70° , respectively. Red and blue arrows represent the incident and reflective directions, respectively, with θ_{diff} denoting their angular difference. (g)–(l) The corresponding far-field radiation patterns.

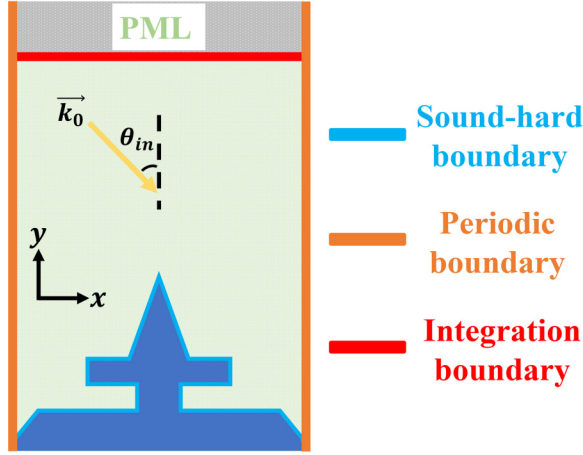


FIG. 6. Setup of the numerical simulation in COMSOL Multiphysics.

are directed only along several discrete directions, instead of along a continuum of directions, which matches well with our optimization objectives. Furthermore, the efficiency curve for each reflection order usually takes a smooth peaklike shape with maximum at its central angle θ_{in} , determined by the formula $\theta_{in} = \arcsin(\frac{-m}{2} \cdot \frac{\lambda}{d})$. Therefore, if we can enhance the reflection efficiency at a single angle θ_{in} for each diffraction order, we can simultaneously increase the reflection efficiencies at nearby incident angles. This is the underlying reason why we can realize a wide-angle retroreflection functionality by considering only a few optimization objectives.

Of course, the simultaneous optimization of seven distinct objectives is far from trivial. We utilize the MOO algorithm for the following reasons. Firstly, the MOO algorithm can handle the tradeoffs between conflicting objectives and find an optimal solution that equally satisfies all objectives. The reflection efficiencies for different diffraction orders indeed have conflicts with each other, especially when one particular θ_{in} corresponds to two neighboring diffraction channels that have an overlapped range of reflection angles. In such a circumstance, enhancing the reflection efficiency of one order would inevitably degrade the reflection efficiency of the other order. For example, the incident angle ranges are $13.7^\circ \leq \theta_{in} \leq 23.6^\circ$ for the -3 rd diffraction order and $20.3^\circ \leq \theta_{in} \leq 30.2^\circ$ for the -4 th diffraction. Thus, in the overlapped range of $20.3^\circ \leq \theta_{in} \leq 23.6^\circ$, enhancing the reflection efficiency of the -3 rd order would inevitably degrade the reflection efficiency of the -4 th order due to the conservation law of wave energy. It is quite difficult for a single-objective optimization algorithm to handle such tradeoffs between different diffraction orders, and this is the underlying reason why we resort to a MOO algorithm. More interestingly, in this paper, we show that, in conjunction with a deep learning predicting model, the MOO algorithm can handle the inverse design problem of a wide-angle retroreflector with satisfying performance and greatly reduced costs of data and time.

V. CONCLUSIONS

In this paper, we propose an alternative and efficient approach to realize a wide-angle high-performance acoustic

retroreflector, which is based on the framework of metagrating. By developing and training a deep learning network PNN and integrating it with the MOO algorithm NSGA-III, we can intelligently utilize the seven different diffraction orders of the metagrating to promptly resolve the inverse design problem. To be more specific, the smartly designed retroreflector can work efficiently over a broad and continuous range of incident angles $13.7^\circ \leq |\theta_{in}| \leq 78.7^\circ$ with pretty high average efficiency. Furthermore, the optimized metagrating has a simple structure and planar configuration, which is easy for fabrication and integration. In addition, the proposed comprehensive NSGA-III + PNN framework shows substantially enhanced optimization efficiency and effectiveness over a huge parameter space and can be utilized for the design of other acoustic devices in various application scenarios.

ACKNOWLEDGMENT

This paper is supported by the Guangdong Basic and Applied Basic Research Foundation (No. 2021A1515010322).

APPENDIX A: DEFINITION AND CALCULATION OF THE REFLECTION EFFICIENCY

In this appendix, we give the definition and calculation method of R_m , the reflection efficiency of the m th diffraction order. For an impinging plane wave with incident angle θ_{in} , we calculate the reflection efficiency R_m with COMSOL by computing the integration of the scattered pressure wave field on the upper boundary (marked by the red line in Fig. 6) of the unit-cell. As shown in Fig. 6, the integration boundary is parallel to the x direction, and periodic boundary conditions are specified on the left and right boundaries (orange lines) that are parallel to the y direction.

The pressure field of the incident plane wave is $p_{in} = b_0 \exp[ik_0(\sin|\theta_{in}|x - \cos|\theta_{in}|y)]$, where $k_0 = 2\pi/\lambda_0$ is the wave number in air. Thus, the energy flux along the y direction is given by $P_{in} = \frac{1}{2} \int p_{in} v_{y,in}^* dx = \frac{1}{2} \frac{-k_0 \cos|\theta_{in}|}{\omega \rho_0} \int |p_{in}|^2 dx$, where a negative sign appears because the plane wave is incident toward the $-y$ direction.

For the m th order reflection wave, its wave vector is given by $\vec{k}_{r,m} = (k_0 \sin|\theta_{in}| + mG, \sqrt{k_0^2 - (k_0 \sin|\theta_{in}| + mG)^2})$, with $G = \frac{2\pi}{d}$. The pressure field and energy flux are, respectively, $p_{r,m} = b_{r,m} \exp[i(k_0 \sin|\theta_{in}| + mG)x] \exp[i\sqrt{k_0^2 - (k_0 \sin|\theta_{in}| + mG)^2}y]$ and $P_{r,m} = \frac{1}{2} \frac{\sqrt{k_0^2 - (k_0 \sin|\theta_{in}| + mG)^2}}{\omega \rho_0} \int |p_{r,m}|^2 dx$. The reflection coefficient $b_{r,m}$ can be calculated by numerical integration on the domain boundary with $b_{r,m} = \int p_{sc}^* \exp[i(k_0 \sin|\theta_{in}| + mG)x] \exp[i\sqrt{k_0^2 - (k_0 \sin|\theta_{in}| + mG)^2}y] dx$. After knowing $b_{r,m}$, we can calculate the energy flux $P_{r,m}$, as well as the m th order reflection efficiency R_m through $R_m = P_{r,m}/P_{in}$.

From above discussions, we can see that R_m refers to the reflection efficiency for the m th diffraction order for any incident angle, and it is not limited to special incident angles such as $\theta_{in} = \arcsin(\frac{-m}{2} \cdot \frac{\lambda}{d})$. Since R_m is normalized with respect

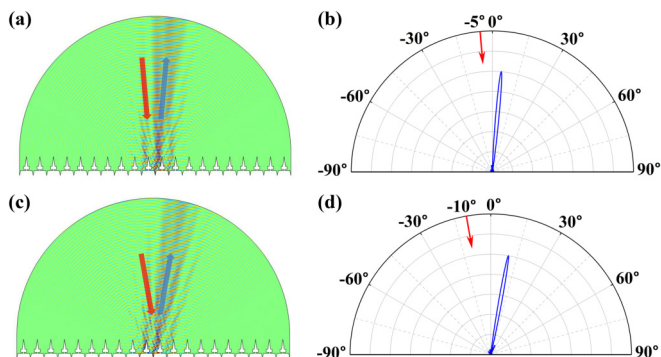


FIG. 7. The performance of the retroreflector at small incident angles. (a) and (c) The scattered pressure field when Gaussian beams are incident at 5° and 10°, respectively. Red and blue arrows represent the incident and reflective directions, respectively. (b) and (d) The corresponding far-field radiation patterns.

to the incident energy flux P_{in} , and $\sum_m R_m$ represent the total energy flux of all reflected orders, we must have $\sum_m R_m = 1$, as dedicated by the law of energy conservation.

APPENDIX B: THE REFLECTION PERFORMANCE AT SMALL INCIDENT ANGLES

In this appendix, we demonstrate the small-angle reflection performance of the retroreflector. In Figs. 7(a) and 7(c), we show the scattered pressure field when the Gaussian beams are incident at 5° and 10°, respectively. Red and blue arrows represent the incident and reflective directions, respectively. The corresponding far-field radiation patterns are shown in Figs. 7(b) and 7(d). It can be observed that the wave beams are reflected along the direction of mirror reflection with $\theta_{re} = \theta_{in}$, where the retroreflection effect ($\theta_{re} = -\theta_{in}$) is missing. This is consistent with what we expected because we do not optimize the reflection performance for $\theta_{in} < 13.7^\circ$ at the first place.

APPENDIX C: THE SHAPE OF THE UNIT-CELL

Basically speaking, each unit-cell of the metagrating contains a resonant cavity, decorated with a triangle groove at the bottom of each cavity and a triangle peak between neighboring cavities. In this way, the interaction of the incident wave and the unit-cell can be efficiently manipulated so that up to seven diffraction channels can be simultaneously controlled.

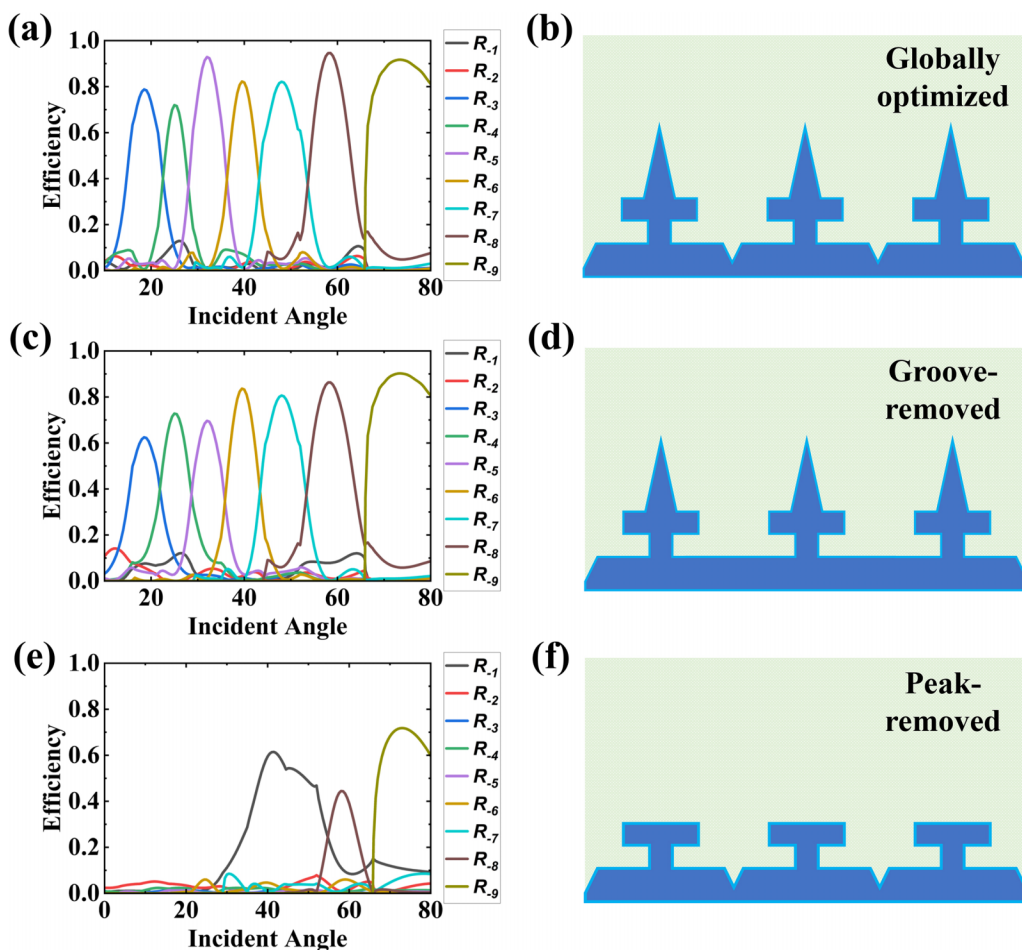


FIG. 8. The comparison of retroreflection responses of three different configurations. (a) and (b) The globally optimized configuration, whose performance is presented in Fig. 3. (c) and (d) The groove-removed configuration. (e) and (f) The peak-removed configuration.

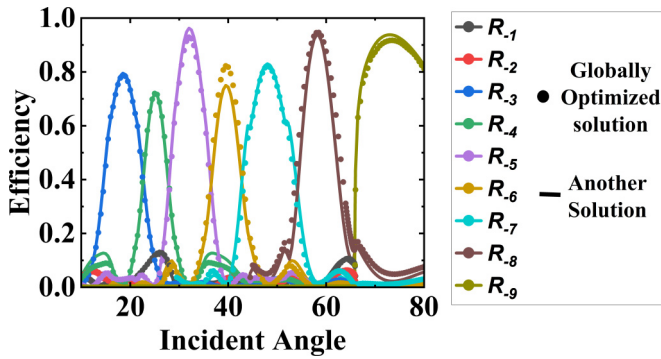


FIG. 9. The retroreflection performance of a locally optimized solution found by the many-objective optimization (MOO) + predicting neural network (PNN) framework. Dotted and solid lines represent the diffraction efficiency spectra of the globally optimized solution and one locally optimized solution, respectively.

In Fig. 8, we compare the retroreflection performances of three different configurations, i.e., (a) and (b) for the globally optimized one (whose performance is presented in Fig. 3), (c) and (d) for the groove-removed one, and (e) and (f) for the peak-removed one. By comparing Fig. 8(c) with Fig. 8(a), we can observe that, when the groove is removed from each resonant cavity, the overall retroreflection efficiencies along seven diffraction channels are substantially lowered, especially for small incident angles where $15^\circ \leq \theta_{in} \leq 35^\circ$. As for the peak-removed configuration that is shown in Fig. 8(e), the overall retroreflection efficiency is far away from what we expect from a retroreflector. Thus, the shape of the unit-cell is specifically designed and optimized to enhance the retroreflection efficiency as much as possible over a broad range of incident angles.

APPENDIX D: COMPARISON BETWEEN THE GLOBALLY AND LOCALLY OPTIMIZED SOLUTIONS

As mentioned in the main text, the MOO + PNN model can find multiple optimized solutions. The performance of the globally optimized solution is demonstrated in Fig. 3, where the reflection efficiencies are 78.8, 72.1, 92.8, 82.4, 82.2, 94.7, and 91.7% at the exact retroreflection angles of $\theta_{in}^{exa} = 18.6^\circ, 25.2^\circ, 32.1^\circ, 39.6^\circ, 48.1^\circ, 58.2^\circ, \text{ and } 73.0^\circ$, respectively. Its diffraction efficiency spectra are plotted as dotted lines in Fig. 9, where the averaged retroreflection efficiency over the seven incident angles is 85.0%.

As a comparison, in Fig. 9, we also plot the retroreflection response of a locally optimized solution found by the MOO + PNN framework, with the corresponding design parameters being $w_1 = 0.0864m, w_2 = 0.4343m, w_3 = 0.1442m, w_4 = 0.2029m, h_1 = 0.0883m, h_2 = 0.2304m, h_3 = 0.3568m, \text{ and } h_4 = 0.7028m$. Its diffraction efficiency spectra are plotted by solid lines, with the corresponding reflection efficiency being 78.9, 72.0, 96.2, 75.4, 82.4, 94.5, and 93.3%, respectively, at the seven exact retroreflection angles. The averaged retroreflection efficiency over the seven incident angles is 84.7%, slightly lower than the globally optimized one.

Furthermore, we note that the globally optimized solution has a more balanced reflection performance over the entire range of θ_{in} , where reflection efficiency along the R_{-6} channel is substantially enhanced (82.4% vs 75.4%), with the price that the reflection efficiency along the R_{-5} channel is slightly lowered.

Thus, the comprehensive MOO + PNN model provides us the flexibility that multiple optimized solutions can be found simultaneously, and all of them have overall satisfying retroreflection performance. We can choose one or several solutions to meet the practical application requirements in various scenarios.

- [1] H. D. Eckhardt, Simple model of corner reflector phenomena, *Appl. Opt.* **10**, 1559 (1971).
- [2] R. Beer and D. Marjaniemi, Wavefronts and construction tolerances for a cat's-eye retroreflector, *Appl. Opt.* **5**, 1191 (1966).
- [3] G. Ma and P. Sheng, Acoustic metamaterials: From local resonances to broad horizons, *Sci. Adv.* **2**, e1501595 (2016).
- [4] S. A. Cummer, J. Christensen, and A. Alu, Controlling sound with acoustic metamaterials, *Nat. Rev. Mater.* **1**, 16001 (2016).
- [5] Y. Fu, J. Li, Y. Xi, C. Shen, Y. Xu, H. Chen, and S. A. Cummer, Compact acoustic retroreflector based on a mirrored Luneburg lens, *Phys. Rev. Mater.* **2**, 105202 (2018).
- [6] B. Yuan, J. Liu, H. Long, Y. Cheng, and X. Liu, Sound focusing by a broadband acoustic Luneburg lens, *J. Acoust. Soc. Am.* **151**, 2238 (2022).
- [7] N. Yu, P. Genevet, M. A. Kats, F. Aieta, J. Tetienne, F. Capasso, and Z. Gaburro, Light propagation with phase discontinuities: Generalized laws of reflection and refraction, *Science* **334**, 333 (2011).
- [8] S. Sun, Q. He, S. Xiao, Q. Xu, X. Li, and L. Zhou, Gradient-index meta-surfaces as a bridge linking propagating waves and surface waves, *Nat. Mater.* **11**, 426 (2012).
- [9] B. Assouar, B. Liang, Y. Wu, Y. Li, J. C. Cheng, and Y. Jing, Acoustic metasurfaces, *Nat. Rev. Mater.* **3**, 460 (2018).
- [10] J. Mei and Y. Wu, Controllable transmission and total reflection through an impedance-matched acoustic metasurface, *New J. Phys.* **16**, 123007 (2014).
- [11] B. Xiong, Y. Liu, Y. Xu, L. Deng, C.-W. Chen, J.-N. Wang, R. Peng, Y. Lai, Y. Liu, and M. Wang, Breaking the limitation of polarization multiplexing in optical metasurfaces with engineered noise, *Science* **379**, 294 (2023).
- [12] A. Arbabi, E. Arbabi, Y. Horie, S. M. Kamali, and A. Faraon, Planar metasurface retroreflector, *Nat. Photonics* **11**, 415 (2017).
- [13] G. Y. Song, Q. Cheng, T. J. Cui, and Y. Jing, Acoustic planar surface retroreflector, *Phys. Rev. Mater.* **2**, 065201 (2018).
- [14] W. Yang, K. Chen, Y. Zheng, W. Zhao, Q. Hu, K. Qu, T. Jiang, J. Zhao, and Y. Feng, Angular-adaptive reconfigurable spin-locked metasurface retroreflector, *Adv. Sci.* **8**, 2100885 (2021).
- [15] X. Song, T. Chen, and J. Zhu, Acoustic reprogrammable metasurface for the multi-frequency tri-channel retroreflector, *Appl. Phys. A* **125**, 679 (2019).
- [16] X. Li, Y. Wang, A. Chen, and Y. Wang, An arbitrarily curved acoustic metasurface for three-dimensional reflected wave-front modulation, *J. Phys. D: Appl. Phys.* **53**, 195301 (2020).
- [17] M. Molerón, M. Serra-García, and C. Daraio, Visco-thermal effects in acoustic metamaterials: From total transmission to

- total reflection and high absorption, *New J. Phys.* **18**, 033003 (2016).
- [18] V. S. Asadchy, M. Albooyeh, S. N. Tsvetkova, A. Díaz-Rubio, Y. Ra'di, and S. A. Tretyakov, Perfect control of reflection and refraction using spatially dispersive metasurfaces, *Phys. Rev. B* **94**, 075142 (2016).
- [19] A. Díaz-Rubio and S. A. Tretyakov, Acoustic metasurfaces for scattering-free anomalous reflection and refraction, *Phys. Rev. B* **96**, 125409 (2017).
- [20] Y. Ra'di, D. L. Sounas, and A. Alù, Metagratings: Beyond the limits of graded metasurfaces for wave front control, *Phys. Rev. Lett.* **119**, 067404 (2017).
- [21] A. M. H. Wong and G. V. Eleftheriades, Perfect anomalous reflection with a bipartite Huygens' metasurface, *Phys. Rev. X* **8**, 011036 (2018).
- [22] D. Torrent, Acoustic anomalous reflectors based on diffraction grating engineering, *Phys. Rev. B* **98**, 060101(R) (2018).
- [23] Y. Fu, C. Shen, Y. Cao, L. Gao, H. Chen, C. T. Chan, S. A. Cummer, and Y. Xu, Reversal of transmission and reflection based on acoustic metagratings with integer parity design, *Nat. Commun.* **10**, 2326 (2019).
- [24] Y. Yang, H. Jia, Y. Bi, H. Zhao, and J. Yang, Experimental demonstration of an acoustic asymmetric diffraction grating based on passive parity-time-symmetric medium, *Phys. Rev. Appl.* **12**, 034040 (2019).
- [25] Z. Hou, X. Fang, Y. Li, and B. Assouar, Highly efficient acoustic metagrating with strongly coupled surface grooves, *Phys. Rev. Appl.* **12**, 034021 (2019).
- [26] Y. K. Chiang, S. Oberst, A. Melnikov, L. Quan, S. Marburg, A. Alù, and D. A. Powell, Reconfigurable acoustic metagrating for high-efficiency anomalous reflection, *Phys. Rev. Appl.* **13**, 064067 (2020).
- [27] L. Fan and J. Mei, Metagratings for waterborne sound: Various functionalities enabled by an efficient inverse design approach, *Phys. Rev. Appl.* **14**, 044003 (2020).
- [28] L. Fan and J. Mei, Acoustic metagrating circulators: Nonreciprocal, robust, and tunable manipulation with unitary efficiency, *Phys. Rev. Appl.* **15**, 064002 (2021).
- [29] L. Fan and J. Mei, Multifunctional waterborne acoustic metagratings: From extraordinary transmission to total and abnormal reflection, *Phys. Rev. Appl.* **16**, 044029 (2021).
- [30] L. Fan and J. Mei, Flow-Permeable and tunable metalens for subdiffraction waterborne-sound focusing, *Phys. Rev. Appl.* **19**, 024026 (2023).
- [31] X. Fang, N. Wang, W. Wu, W. Wang, X. Yin, X. Wang, and Y. Li, Extreme wave manipulation via non-hermitian metagratings on degenerated states, *Phys. Rev. Appl.* **19**, 054003 (2023).
- [32] V. S. Asadchy, A. Díaz-Rubio, S. N. Tsvetkova, D.-H. Kwon, A. Elsakka, M. Albooyeh, and S. A. Tretyakov, Flat engineered multichannel reflectors, *Phys. Rev. X* **7**, 031046 (2017).
- [33] J. He, X. Jiang, D. Ta, and W. Wang, Experimental demonstration of underwater ultrasound cloaking based on metagrating, *Appl. Phys. Lett.* **117**, 091901 (2020).
- [34] Y. Jin, X. Fang, Y. Li, and D. Torrent, Engineered diffraction gratings for acoustic cloaking, *Phys. Rev. Appl.* **11**, 011004 (2019).
- [35] A. Song, C. Sun, Y. Xiang, and F. Z. Xuan, Switchable acoustic metagrating for three-channel retroreflection and carpet cloaking, *Appl. Phys. Express* **15**, 024002 (2022).
- [36] C. Shen, A. Díaz-Rubio, J. Li, and S. A. Cummer, A surface impedance-based three-channel acoustic metasurface retroreflector, *Appl. Phys. Lett.* **112**, 183503 (2018).
- [37] X. Li, D. Dong, J. Liu, Y. Liu, and Y. Fu, Perfect retroreflection assisted by evanescent guided modes in acoustic metagratings, *Appl. Phys. Lett.* **120**, 151701 (2022).
- [38] J. C. Hsu, H. Alwi, C. H. Wei, K. L. Liao, and C. T. Huang, Reflections of high-frequency pulsed ultrasound by underwater acoustic metasurfaces composed of subwavelength phase-gradient slits, *Crystals* **13**, 846 (2023).
- [39] L. S. Zeng, Y. X. Shen, X. S. Fang, Y. Li, and X. F. Zhu, Experimental realization of ultrasonic retroreflection tweezing via metagratings, *Ultrasonics* **117**, 106548 (2021).
- [40] Y. Ruan, X. Liang, and C. Hu, Retroreflection of flexural wave by using elastic metasurface, *J. Appl. Phys.* **128**, 045116 (2020).
- [41] S. Bernard, F. Chikh-Bled, H. Kourchi, F. Chati, and F. Léon, Broadband negative reflection of underwater acoustic waves from a simple metagrating: Modeling and experiment, *Phys. Rev. Appl.* **17**, 024059 (2022).
- [42] Y. Fu, Y. Cao, and Y. Xu, Multifunctional reflection in acoustic metagratings with simplified design, *Appl. Phys. Lett.* **114**, 053502 (2019).
- [43] M. Li, L. Jing, X. Lin, S. Xu, L. Shen, B. Zheng, Z. Wang, and H. Chen, Angular-adaptive spin-locked retroreflector based on reconfigurable magnetic metagrating, *Adv. Opt. Mater.* **7**, 1900151 (2019).
- [44] J. Jiang, M. Chen, and J. Fan, Deep neural networks for the evaluation and design of photonic devices, *Nat. Rev. Mater.* **6**, 679 (2021).
- [45] J. Jiang, D. Sell, S. Hoyer, J. Hickey, J. Yang, and J. A. Fan, Free-form diffractive metagrating design based on generative adversarial networks, *ACS Nano* **13**, 8872 (2019).
- [46] N. J. Dinsdale, P. R. Wiecha, M. Delaney, J. Reynolds, M. Ebert, I. Zeimpekis, D. J. Thomson, G. T. Reed, P. Lalanne, K. Vynck *et al.*, Deep learning enabled design of complex transmission matrices for universal optical components, *ACS Photonics* **8**, 283 (2021).
- [47] W. W. Ahmed, M. Farhat, X. Zhang, and Y. Wu, Deterministic and probabilistic deep learning models for inverse design of broadband acoustic, *Phys. Rev. Res.* **3**, 013142 (2021).
- [48] Z. Du and J. Mei, Metagrating-based acoustic wavelength division multiplexing enabled by deterministic and probabilistic deep learning models, *Phys. Rev. Res.* **4**, 033165 (2022).
- [49] S. D. Campbell, D. Sell, R. P. Jenkins, E. B. Whiting, J. A. Fan, and D. H. Werner, Review of numerical optimization techniques for meta-device design, *Opt. Mater. Express* **9**, 1842 (2019).
- [50] K. Deb and H. Jain, An evolutionary many-objective optimization algorithm using reference-point-based nondominated sorting approach, part I: Solving problems with box constraints, *IEEE Trans. Evol. Computat.* **18**, 577 (2014).